frontiers | Frontiers in Materials

TYPE Original Research
PUBLISHED 06 February 2025
DOI 10.3389/fmats.2025.1545242

OPEN ACCESS

EDITED BY
Caizhi Zhou,
University of South Carolina, United States

REVIEWED BY
Pavlo Maruschak,
Ternopil Ivan Pului National Technical University, Ukraine
Xiaodong Tan,
Southwest University, China

*CORRESPONDENCE
Xiurong Zuo,
zuoxiurong@zzu.edu.cn

RECEIVED 14 December 2024
ACCEPTED 20 January 2025
PUBLISHED 06 February 2025

CITATION
Tong K, Sun H, Duan L and Zuo X (2025) Influence of TiN inclusions and segregation bands on the mechanical properties and ballistic performance during ballistic impact tests in low-alloy high-strength steel. *Front. Mater.* 12:1545242. doi: 10.3389/fmats.2025.1545242

Influence of TiN inclusions and segregation bands on the mechanical properties and ballistic performance during ballistic impact tests in low-alloy high-strength steel

Keke Tong, Haoran Sun, Luxing Duan and Xiurong Zuo*

Key Laboratory of Materials Physics, Ministry of Education, School of Physics, Zhengzhou University, Zhengzhou, China

The influence of TiN inclusions and segregation bands on the mechanical properties and ballistic performance was investigated in high-strength steel. With ballistic test at a bullet impact velocity of about 810 m/s, the steel plate displayed the different ballistic performance, forming partially penetrated crater A and the completely penetrated crater B, despite the craters A and B were close together with only about 100 mm. The zone near crater A displayed excellent strength, plasticity and deformability than that near crater B. The segregation bands and TiN inclusions in steel plate originated from central segregation in continuous casting slabs. The Adiabatic shear bands (ASBs) with total length of 14,848 μm around crater B was more serious than that with total length of 6,239 μm around crater A, attributed to the low *n* value and strain hardening rate in completely penetrated crater region. Cracks parallel to the penetration direction only occurred around the crater B. Cracks also formed along the interfaces of ASB and matrix. The inhomogeneous deformation around ASBs resulted in stress concentration, especially at the interface between the matrix and the segregation band, making the long crack initiation and propagation under load of impact.

KEYWORDS

low-alloy high-strength steel, segregation band, TiN inclusion, mechanical property, ballistic performance

1 Introduction

As a preferred material for ballistic protection applications, high-strength martensitic steel has become a focal point of research, due to excellent mechanical properties, such as high strength and excellent plasticity which can satisfy the increasing demands for safety against ballistic impact (Yilmaz, 2010; McDonald et al., 2019; Singh et al., 2019).

Adiabatic shear band (ASB) represents one of the primary failure modes in armored steel during ballistic testing, which is primarily induced by the competition between strain hardening and thermal softening effects during high-velocity impacts, leading to

thermomechanical instability in the material (Baik et al., 2021). The occurrence of ASB is also associated with material defects. The presence of banded microstructures, boundaries and non-metallic inclusions disrupts the microstructure uniformity (Narasaiah and Ray, 2005; Bee et al., 2023). In high-velocity impact process, significant uneven deformation in matrix results in stress concentration, especially at the boundaries of grain, placket, block, lath of martensite and the interface of segregation/matrix and inclusion/matrix. That is to say, under applied external forces, ASBs along with cracks are more likely to develop at these heterogeneous locations, leading to a reduction in the mechanical properties and ballistic performance of the material. A high strain hardening exponent (n) and strain hardening rate can restrained the localized deformation and the final formation of ASB (Jo et al., 2020)

The segregation bands originate from the enrichment of solute during solidification process. During deformation, segregation bands display a higher plastic deformation resistance, so only a small deformation degree can occur. Whereas a large deformation degree occurs in matrix. In a word, the existence of the strain gradient between matrix and segregation promotes the crack initiation (Wang et al., 2020; Zhang et al., 2022). Coarse TiN inclusions in steel can lead to the fluctuation in impact toughness, as TiN inclusions disrupt the continuity of the matrix, resulting in micro-crack propagation. However, the refinement in ferrite grains and TiN size can improve the uniformity of the impact properties of the steel plates (Liu et al., 2018).

Extensive research has been done on the effects of the inhomogeneous microstructures, which was caused by segregation bands and TiN inclusions, on mechanical properties of high-strength steel during the quasi-static loading condition (Wu et al., 2020; Liu et al., 2022). However, the influence of inhomogeneous microstructures on the ballistic performance subjected to the high-velocity impact need to be intensively studied, in order to restrain the ASBs and cracks formation during the dynamic loading condition, thereby high-strength low alloy steel with high-ballistic performance can be successfully developed.

After ballistic test, the partially penetrated crater and completely penetrated crater with only about 100 mm distance between them were found in the steel plate in this study. Therefore, the aim of the present work was to study the effect of the microstructure uniformity on ballistic performance of high strength steel. Firstly, the microstructure, i.e., TiN inclusions, grain size and segregation band, on the mechanical properties of high strength steels was studied in the area between the partially penetrated crater and completely penetrated crater. And then, formation mechanism of ASB and cracks during ballistic impact process was also discussed, thereby offering significant theoretical insights and practical guidance for enhancing the performance of armored steel.

2 Materials and methods

The experimental material in this study was a 12 mm thick low-alloy high-strength steel plate (Fe-0.33C-0.48Mn-0.20Si-0.37Cr-0.09Mo-0.008Ti-0.016Nb-0.0013B (wt%)), which was obtained by thermo-mechanical control process from 150 mm thickness slab. Subsequently, steel plate was quenching at 880 °C and tempered at 180°C, whose microstructure consisted mainly of tempered martensite and bainite. With ballistic test at a bullet impact velocity of about 810 m/s, and the distance between the gun and the target plate was 100 m, the steel plate was partially penetrated forming crater A and completely penetrated forming crater B (Figure 1A), despite the craters A and B are close together with only about 100 mm. Two craters A and B were half-sectioned by an electric spark wire cutting machine to observe the ballistically-impacted microstructure around the craters using multiscale approach at macroscale, mesoscale, and microscale (Maruschak and Maruschak, 2024). After etching the polished specimens with 4% Nital or picric acid, ASB, segregation bands, and grains were observed around the craters by an optical microscopy (OM; Axiolab 5, ZEISS, Germany). TiN inclusions in initial steel plate were observed using OM. After etching with picric acid, the grain sizes in initial steel plate were statistically counted using OM.

According to the GB/T 228.1-2021 standard (China National Standard, 2021), cylindrical specimens with a gauge length of 30 mm and a diameter of 6 mm were extracted between crater A and crater B in steel plate (Figure 1B). Room temperature tensile tests were conducted at a speed of 10 mm/min using a universal testing machine (CMT5105, SANS, China). Ultra-depth-of-field 3D microscope (DSX1000, Olympus, Japan) was used to reveal the differences in the fracture shapes of the tensile specimens. Subsequently, three representative specimens were selected for analysis of the fracture surfaces by scanning electron microscopy (SEM; JSM 6700F, JEOL, Japan) and energy dispersive spectrometer (EDS; INCA-ENERGY, Oxford, United Kingdom). After etching the polished specimens with 4% Nital, microhardness testing was conducted with a 0.3 kg testing force (XHD-2000TMSC, Vickers, China).

Elemental analysis of the micro-area composition was conducted using Electron Microprobe Analysis (EPMA-8050G, Shimadzu, Japan). An electron backscattered diffractometer (EBSD) analysis was performed on a dual-beam SEM (Helios G4 CX, Thermo Fisher Scientific, Czech Republic) equipped with an EBSD detector, operating at 20 kV with a scan step of 0.2 μm. The specimen for EBSD was polished using a multi-functional ion thinning instrument (Leica EM Res102, Leica, Germany). Data acquisition and processing were performed using HKL Channel 5 software.

3 Results

3.1 Macroscopic and microscopic morphology of the cross-section of craters

In the ballistic experiment, bullets were vertically shot toward the target plate. The macroscopic and microscopic morphology of the half-sectioned area of the craters etched in 4% Nital or picric acid were showed in Figure 2. Figure 2A showed the bullet head conically recessed into the target plate forming the partially penetrated crater A with a depression on the front face and a slight bulge on the rear face. Figure 2B showed the completely perforated target plate, forming the crater B.

Further observation for the microscopic morphology was conducted using OM. After being corroded by 4% Nital, the projectile and the base showed two different morphologies (Figure 2C). White ASBs formed around the crater A (white arrows

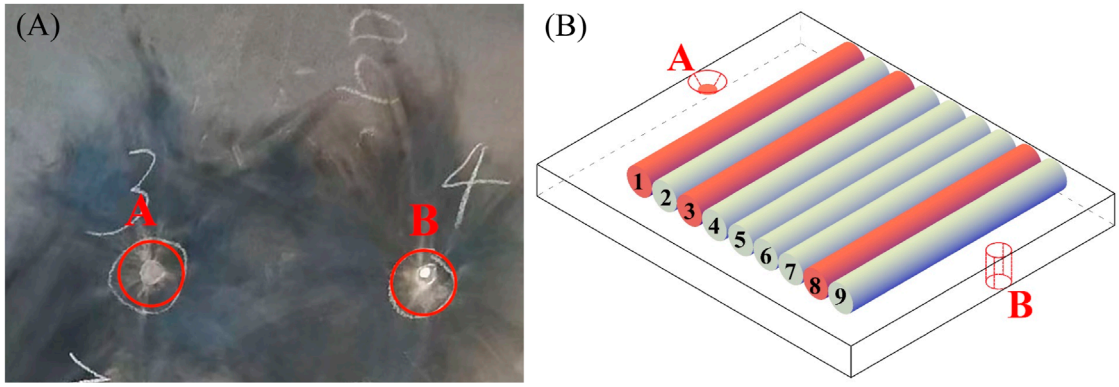

FIGURE 1
(A) Steel plate after bullet penetration test, and **(B)** Schematic diagram of sampling for tensile test specimen.

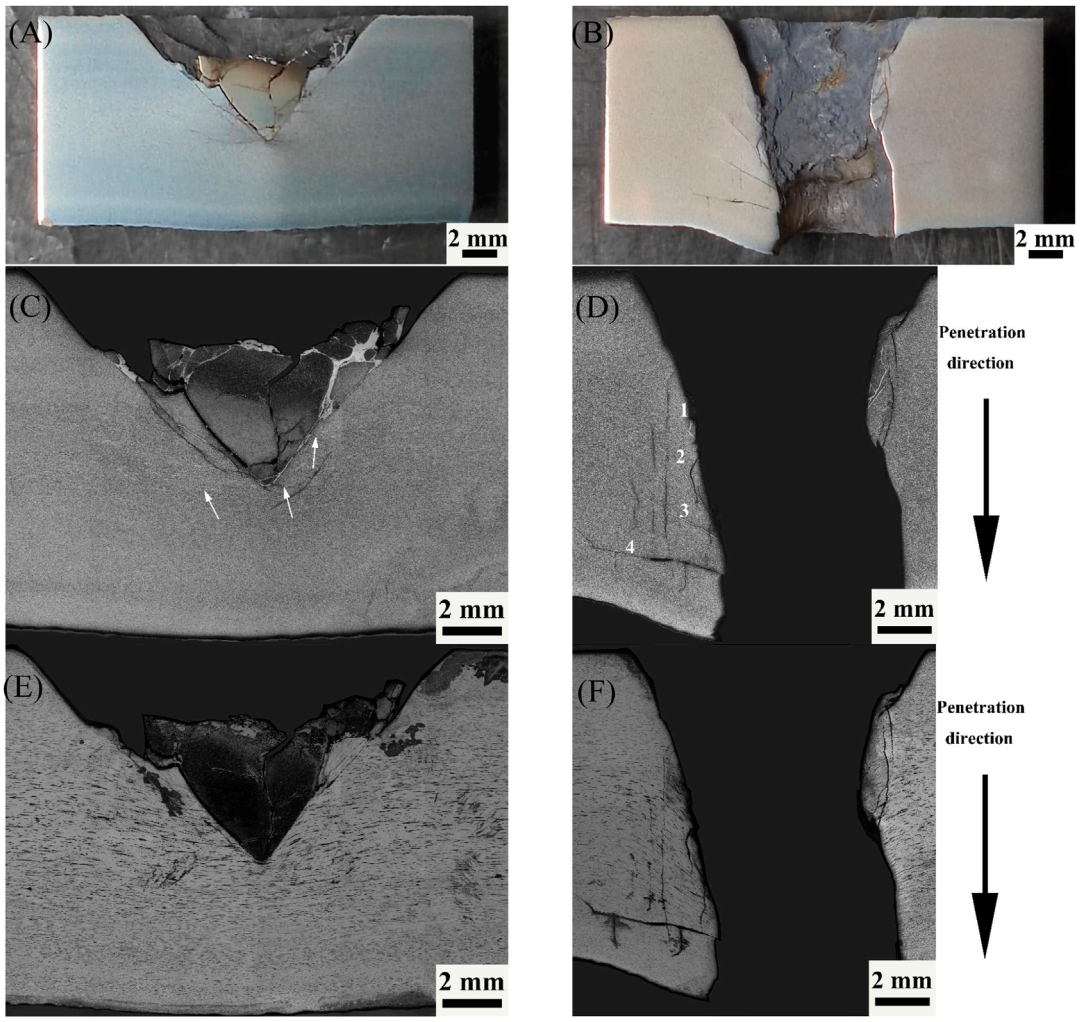

FIGURE 2
The macroscopic and microscopic morphology of the half-sectioned area of the craters etched in 4% Nital or picric acid. **(A, B)** Macroscopic morphology of craters A and B (Nital etching), **(C, D)** OM images of craters A and B by Nital, and **(E, F)** OM images of craters A and B by picric acid.

in Figure 2C) and crater B. Generally, cracks tended to propagate along these ASBs. Cracks on both sides of the craters were observed (Figures 2C, D). However, more cracks were observed around crater B than those of crater A (Borvik et al., 2002). The cracks around crater B exhibited not only orienting at a 45-degree angle to the penetration direction but also parallel to the penetration direction. At the same time, there were more and longer ASBs around the crater B (numbered 1,2,3,4 in Figure 2D). The ASB was formed under high-speed impact, which had the propensity to induce crack nucleation and subsequent propagation along these ASBs, thereby serving as a primary factor contributing to the failure of steel plates. The generation of ASB may be associated with factors such as the intrinsic material properties, structural homogeneity, and the presence of internal defects in the target plate material (Singh et al., 2019; Singh et al., 2021).

After etching with picric acid, as shown in Figures 2E, F, the microstructure around two craters showed heavy deformation in the segregation bands around the craters. The deformation around the completely penetrated crater B was much more serious than that around the partially penetrated crater A.

3.2 Mechanical properties

According to (Chausov et al., 2024), the dynamic non-balanced processes, such as dynamic destruction, may cause changes in the mechanism of plastic deformation. However, the static tensile still have reference significance. The ballistic performance of high-strength steel is correlated with its mechanical properties. Target plates with high hardness, high strength and excellent ductility show superior resistance to penetration necessitating (Borvik et al., 2009; McDonald et al., 2019). Therefore, tensile specimens were selected between the locations of the thoroughly penetrated crater B and the partially penetrated crater A on the target plate, as shown in Figure 1B.

From Figure 3A, it was found that tensile properties showed significant difference, despite virtually same location. The yield strength of the steel plate exceeded 1,400 MPa and the tensile strength exceeded 1,700 MPa. The strength of the specimens 1,2,3,4 near crater A was slightly higher than those near crater B (specimens 6,7,8,9), at the same time, the elongation and n value of the former was higher than that of the latter, indicating excellent strength, plasticity and deformability near the crater A zone. The fracture surface shapes in the inset of Figure 3A displayed diversity, indicating the difference in microstructure of each tensile specimen. Compared to the fracture surfaces of specimens 1,2,3,4, the tensile fracture surface of the specimens 6,7,8,9 seemed more irregular in shape.

To explore the reasons, typical engineering stress-strain curves were displayed in the Figure 3B. The stress-strain curves of specimen 1 near crater A, specimen 3 in the middle, and specimen 9 near crater B, which was indicated by red color in Figure 1B, displayed evident differences. Specimens 1 and 3 exhibited excellent elongation compared to specimen 9. During the tensile process, interactions of dislocations resulted in work hardening, which was characterized by the strain hardening rate and the n value (Zhang et al., 2010). The greater the n value indicated the higher work hardening. In order to describe the strain hardening behavior of materials, the true stress (σ) - true strain (ε) curves are derived from the engineering stress-engineering strain curves using Equations 1, 2.

$$\boldsymbol{\sigma} = \boldsymbol{s} \times (\mathbf{1} + \boldsymbol{e}) \tag{1}$$

$$\boldsymbol{\varepsilon} = \mathbf{ln}\,(\mathbf{1} + \boldsymbol{e}) \tag{2}$$

where e is the engineering strain, s is the engineering stress.

The strain hardening rate curve in Figure 3C is obtained by differentiating the σ-ε curve of the plastic region.

n value is calculated using the Hollomon equation as follows:

$$\boldsymbol{\sigma} = \boldsymbol{K}\boldsymbol{\varepsilon}^{\boldsymbol{n}} \tag{3}$$

where K is the strength coefficient.

Taking the logarithm on both sides of Equations 3, 4 was obtained.

$$\mathbf{ln}\,\boldsymbol{\sigma} = \mathbf{ln}\boldsymbol{K} + \boldsymbol{n}\,\mathbf{ln}\,\boldsymbol{\varepsilon} \tag{4}$$

$$\boldsymbol{n} = \frac{\mathbf{d\,ln}\,\boldsymbol{\sigma}}{\mathbf{d\,ln}\,\boldsymbol{\varepsilon}} \tag{5}$$

By examining the n - ε curves based on Equation 5 in Figure 3D, it was observed that the instantaneous n values for specimens 1 and 3 were significantly higher than that of specimen 9, indicating that the excellent deformability of specimens 1 and 3. At the same time, with the increase of ε, the n values decreased gradually, due to the dynamic recovery caused by cross-slip with dislocations pile-up.

3.3 Fracture morphologies

Through SEM analysis of the fracture morphologies of specimens 1, 3, 9 in Figure 4, it was observed that the fracture surfaces were composed of fiber regions and shear lips. Figures 4A, B, C showed the macroscopic fracture surface. Separation cracks with varied location were found in fiber regions, making the fracture shapes different, which indicated the inhomogeneity of microstructure, especially the distribution of segregation bands. As shown in Figures 4D–F, a large number of dimples and a few cleavage facets were found on the fiber regions. In addition, some deep dimples were found which are typical characteristics of ductile fracture. However, the shear lips of the three specimens showed shallow dimples with shear characteristics and a few cleavage surfaces (Figures 4G–I), furthermore, more cleavage surfaces were found in specimen 9 (Figure 4I).

The inclusion with regular shape in Figure 4J was identified as ((Nb, Ti) (C,N)) by EDS analysis in the Figure 4K, due to the epitaxial growth of NbC on TiN particles in the rolling (Ma et al., 2017). Smooth cleavage surfaces surrounding these inclusions were found, indicating the characteristics of brittle failure. During the tensile process, the presence of large-sized TiN inclusions was prone to inducing crack, which led to brittle failure and ultimately reduced the material plasticity.

Based on the above analysis, it was evident that the plasticity of specimen 1 near the crater A on the target plate was higher than specimen 9 near carter B. Consequently, it was believed that the differences in the ballistic test results of the target plate might be attributed to the inhomogeneity of microstructure and properties.

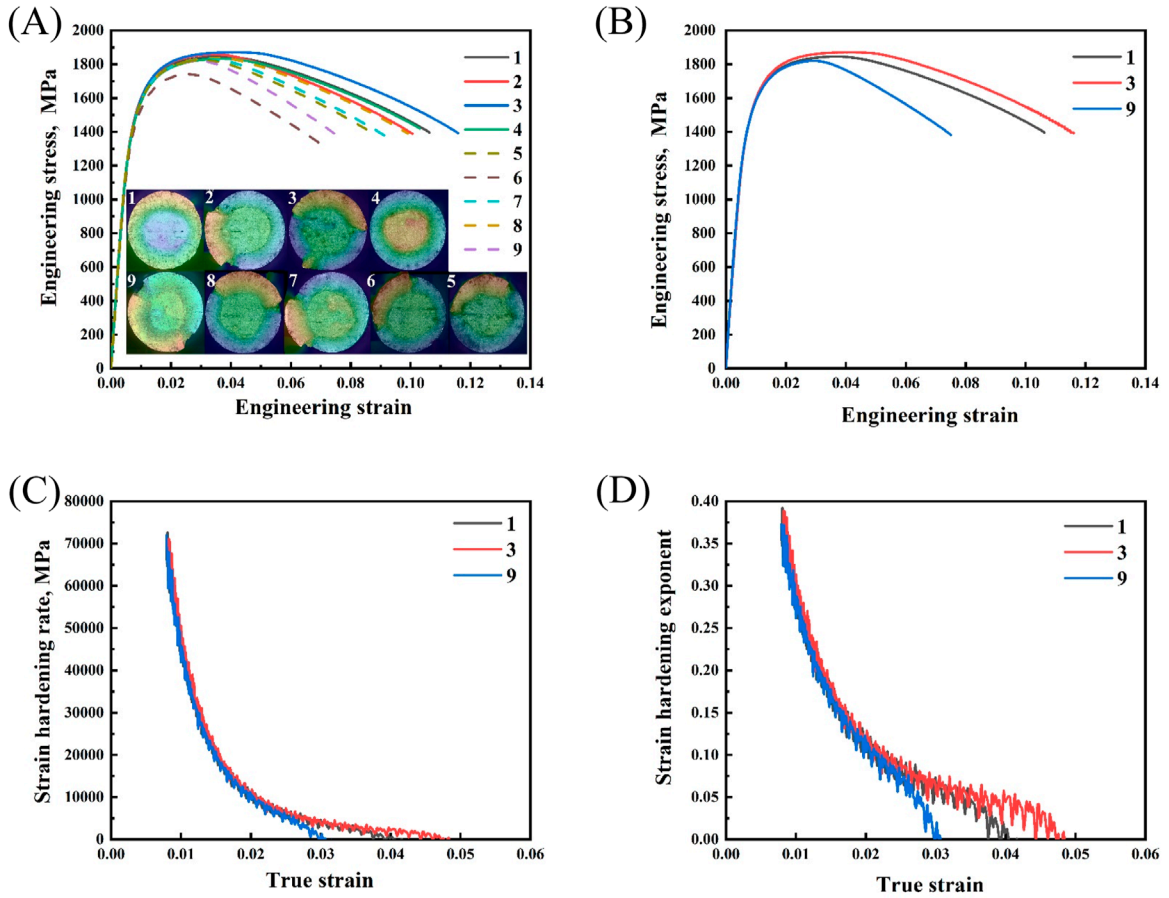

FIGURE 3
(A) Overall stress-strain curve, **(B)** Stress-strain curves of specimens 1, 3, and 9, **(C)** Strain hardening rate curve, **(D)** Strain hardening exponent curve.

Furthermore, the presence of TiN inclusions was likely to be one of the reasons deteriorating the plasticity of the target plate.

3.4 Microstructure

The microstructure has an impact on the mechanical properties of materials. An analysis of the differences in microstructure was conducted by comparing the specimens 1, 3 and 9 in clamping ends of tensile specimens. The Figures 5A–C illustrated the central segregation etched with picric acid. It can be observed that the distribution of segregation bands was inhomogeneous, whose lengths and widths varied throughout the entire field of view. Some of them were narrow and light, and others were thick and dark. This kind of phenomenon was particularly pronounced in specimen 9.

The line scanning results by EPMA, as shown in Figure 5D, showed three distinct peaks in elemental content which corresponded to specific locations in the segregation band. It was evident that the segregation band exhibited obvious C enrichment, and slight enrichment of Mn and Cr, compared to the surrounding matrix, which increased the solution strengthening effect in segregation band.

After etching with picric acid, the grain sizes in specimen 3 were measured, as shown in Figure 5F. It was found that the grain sizes on the segregation bands were smaller than those in the matrix. The maximum grain size of matrix between bands exceeded 30 μm, while that on the bands did not exceed 20 μm. The average grain sizes and standard deviations of segregation bands and matrix were 5.67 μm and 3.15 μm, 7.57 μm and 4.73 μm, respectively. Evidently, grain refinement occurred in the segregation band, as the element enrichment in the segregation band delayed the phase transition (Teixeira et al., 2021; Wang et al., 2022). Studies have shown that grain refinement can enhance the strength and hardness of materials (Bertolo et al., 2023; Liang et al., 2023), hence resulting in higher hardness values on the segregation band compared to the matrix.

From Figure 5E, the microstructure on the segregation bands consisted of martensite with higher hardness values (619 HV). In the matrix near the segregation bands, a significant decrease in hardness (590 HV and 496 HV) was observed, due to the microstructure comprising a mixture of martensite and bainite. The hardness gradient, which existed in matrix and segregation bands, resulted in the significant variations in the fracture morphologies.

In summary, the segregation band with fine grains and solute element enrichment displayed high hardness, compared with the

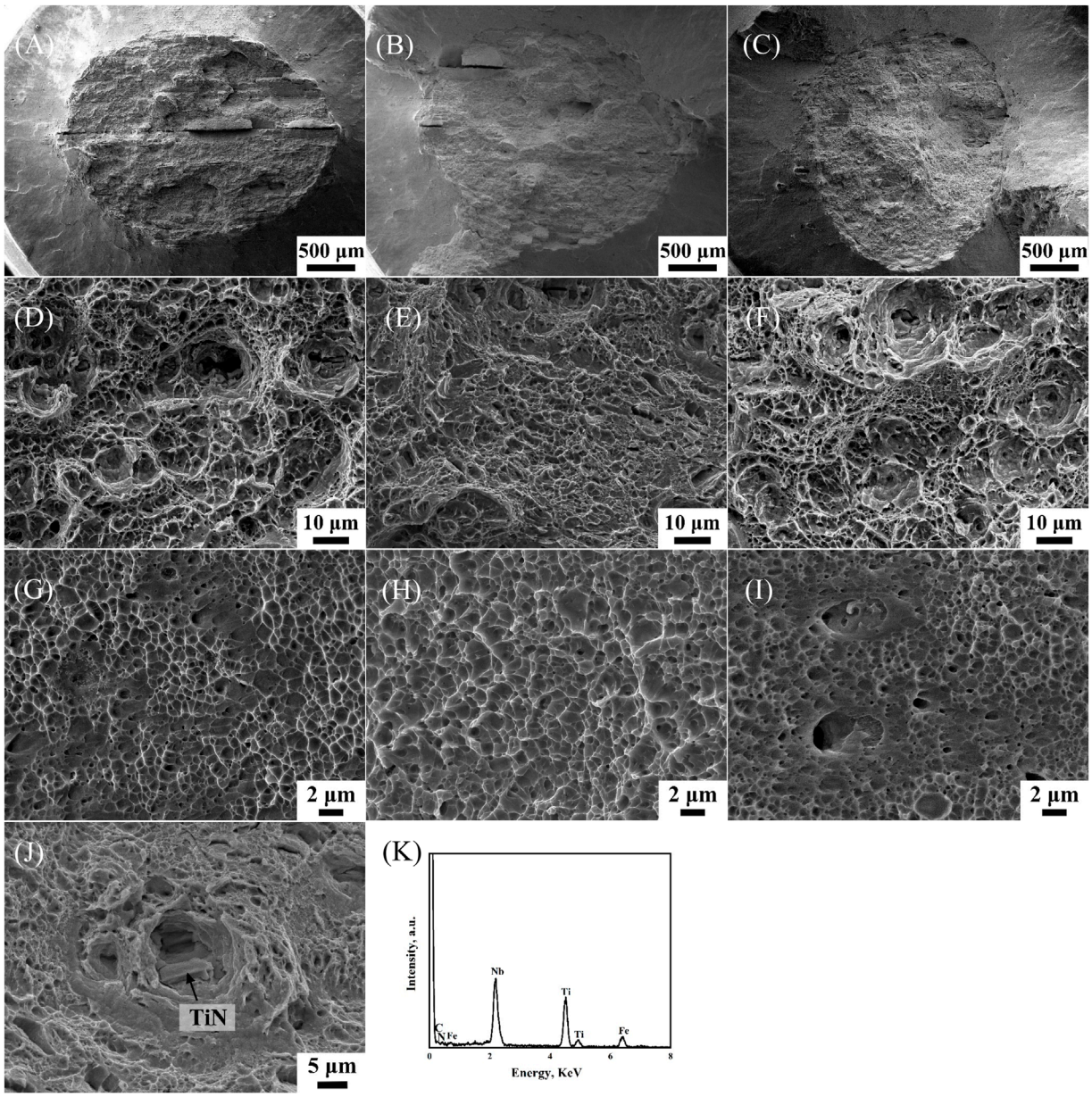

FIGURE 4
SEM images of tensile fracture surfaces. **(A–C)** Macroscopic fracture surfaces of specimens 1, 3 and 9, **(D–F)** Fiber zone of specimens 1, 3 and 9, **(G–I)** Shear lips of specimens 1, 3 and 9, **(J)** TiN inclusion on the fracture surface, and **(K)** EDS of TiN.

surrounding matrix. However, despite a significant difference in hardness between the segregation band and surrounding matrix, the similar strength of specimens 1, 3 and 9 was found. The inhomogeneous distribution of the hard segregation band resulted in varying hardness gradient distribution, whereas the bulk properties of tensile strength displayed the similar values. However, cracks were prone to initiating at the interface between the matrix and the segregation band due to stress concentration during tensile loading, ultimately reducing the plasticity of the steel plate. So specimen 9 with the most uneven segregation band distribution displayed the worst plasticity.

In this study, it was found that the TiN inclusions were almost located on the segregation bands. Figure 6A showed TiN inclusions with homogeneous and heterogeneous nucleation. As shown in Figures 6B, C, F, the heterogeneous nucleation core of TiN inclusion was CaS and MgO by EDS analysis (Wang et al., 2021). Compared with homogeneous-nucleated TiN inclusions, heterogeneous-nucleated TiN inclusions were more prone to initiating crack from soft CaS and MgO cores (He et al., 2022). Chain-like TiN inclusions, which were located in hard segregation bands, were also easy to induce crack due to a superposition of stress fields around TiN inclusions (Figures 6D, E) (Sun et al., 2023).

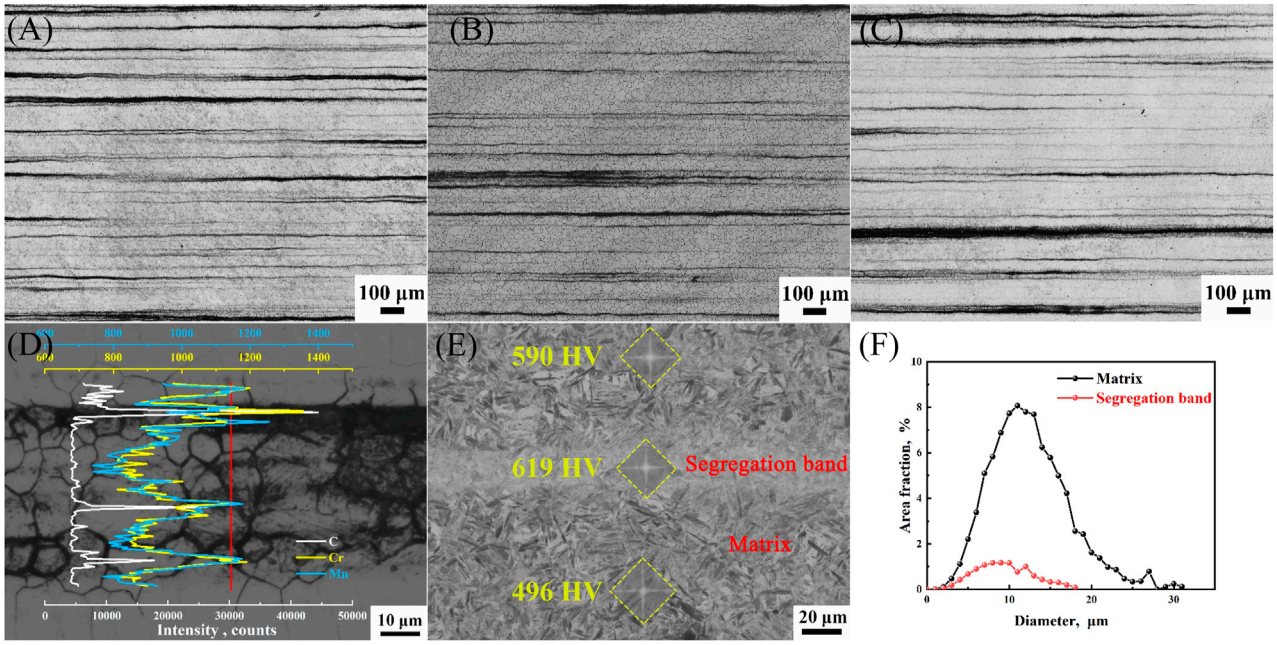

FIGURE 5
(A–C) Segregation bands in specimens 1, 3 and 9, respectively, **(D)** EPMA line scan for segregation band in specimen 3, **(E)** Hardness of matrix and segregation band, and **(F)** Grain distribution in specimen 3.

4 Discussion

4.1 Formation mechanism of segregation band and TiN

The influence of the varied content of Ti and N on the precipitation process of TiN was analyzed based on the thermodynamic formula. Considering the preferential combination of Ti with N, TiN was formed according to Equation 6. The theoretical concentration product of the TiN (K_{TiN}) was shown in Equation 7. The actual concentration product of TiN (Q_{TiN}) in molten steel is expressed by Equation 8.

$$\mathbf{Ti + N = TiN_{inclusion}} \tag{6}$$

$$\log K_{TiN} = \log[Ti] \cdot [N] = -\frac{15218}{T} + 5.64 \tag{7}$$

$$Q_{TiN} = \frac{[Ti]_0[N]_0(1-f_s)^{k_{Ti}}}{1-(1-k_N)\cdot f_s} \tag{8}$$

The concentration of the Ti and N in the solidification front was expressed by Equations 9, 10, respectively.

$$[Ti]_l = [Ti]_0 \times (1-f_s)^{k_{Ti}-1} \tag{9}$$

$$[N]_l = \frac{[N]_0}{(1-(1-k_N)\times f_s)} \tag{10}$$

where $[Ti]_l$, $[N]_l$, $[Ti]_0$, and $[N]_0$ represent the concentrations of Ti and N in the solidification front and their initial concentrations, respectively. k_{Ti} (0.33) and k_N (0.48) represent the equilibrium distribution coefficients of Ti and N, respectively.

From Equations 9, 10, it was found that Ti and N were continuously enriched in the solidification front during the solidification process of molten steel with the increase of solid fraction (f_s), as shown in Figure7A. Until 0.98 f_s, the TiN began to form (Figure 7B). Enrichment of C, Mn, Cr, and Si was found in segregation region in slab center by EPMA, at the same time, TiN inclusions were also found in segregation region in Figure 8.

In other words, the segregation bands in steel plate originated from segregation region in slabs. The segregation region as the final solidification zone during continuous casting contained micro-sized TiN inclusions, which was the reason why almost all TiN located in segregation bands in steel plate after rolling, as shown in Figure 6. Segregation region in slabs was hardly removed by the subsequent reheating, rolling and heat treatment process, and then were ultimately deformed into bands (Guo et al., 2020).

4.2 EBSD analysis of TiN inclusions and segregation bands in initial steel plate

According to the research conducted by (Singh et al., 2021), the boundaries, inclusions, and segregation bands may be the potential initiation sites for ASB and crack formation. Figures 9A, B showed the TiN inclusions located in segregation band. The regions in the black boxes in Figures 9A, B were selected for EBSD analysis. Low-angle (LAGBs, 2°–15°) and high-angle boundaries (HAGBs, >15°) were represented by black and red lines, respectively in Figures 9C, D. At the interfaces of the matrix/segregation bands (the black arrow in Figure 9D), more HAGB was found. Especially for the TiN inclusion, high local strain zone in the sharp corner of

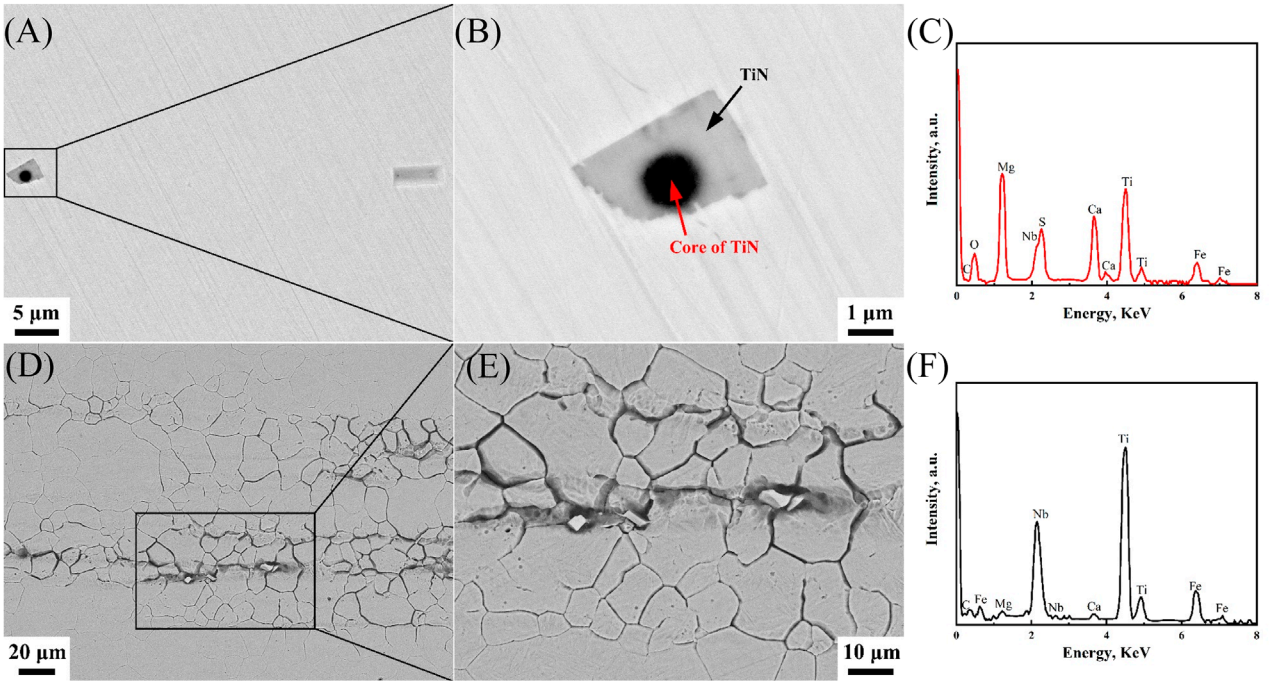

FIGURE 6
The homogeneous and heterogeneous nucleation of TiN, and chain-like TiN inclusions. **(A, B)** TiN inclusions with homogeneous and heterogeneous nucleation, **(D, E)** Chain-like TiN inclusions, **(C, F)** EDS of TiN core (red arrow) and TiN edge (black arrow).

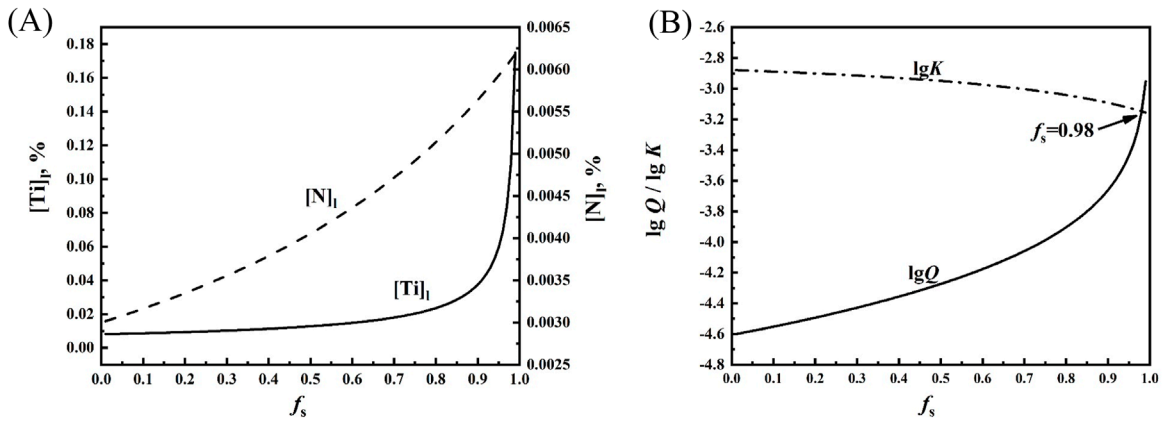

FIGURE 7
Thermodynamic analysis of TiN. **(A)** Increase of the concentrations of Ti and N in the solidification front with the solid fraction (f_s), and **(B)** Relationship between k_{TiN}/Q_{TiN} and f_s.

TiN were found (red arrow in Figure 9D). The crack was prone to preferential initiating at the sharp corner of the TiN inclusion (Shi et al., 2022). The significant difference of thermal expansion coefficient between the γ-Fe matrix and TiN inclusion during quenching cooling resulted in the serious thermal stresses and strains (Pan et al., 2003). Ultimately, a certain plastic zone with high strain would be produced around TiN. In the process of subsequent ballistic impact deformation, elastic or elastic-plastic incompatibility of TiN and matrix might be the primary mechanism for ASBs and cracks initiation (Narasaiah and Ray, 2005). Due to microstructural inhomogeneity, some large grains with high local strain at the boundaries of grain and placket/block/Lath of martensite were found everywhere, which would tend to initiate ASBs and cracks.

4.3 Statistical analysis of ASB and crack

ASBs formed from the severely localized deformation during ballistic impact test. Owing to the absorbing of the ballistic

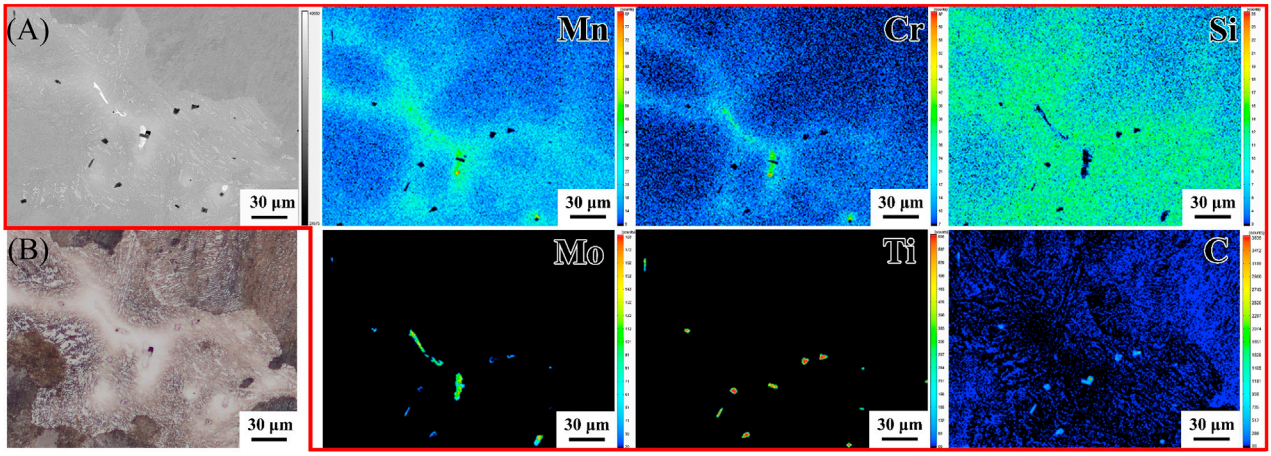

FIGURE 8
OM and EPMA images of central segregation in the central equiaxed crystal zone of slab. **(A)** EPMA images, and **(B)** OM image.

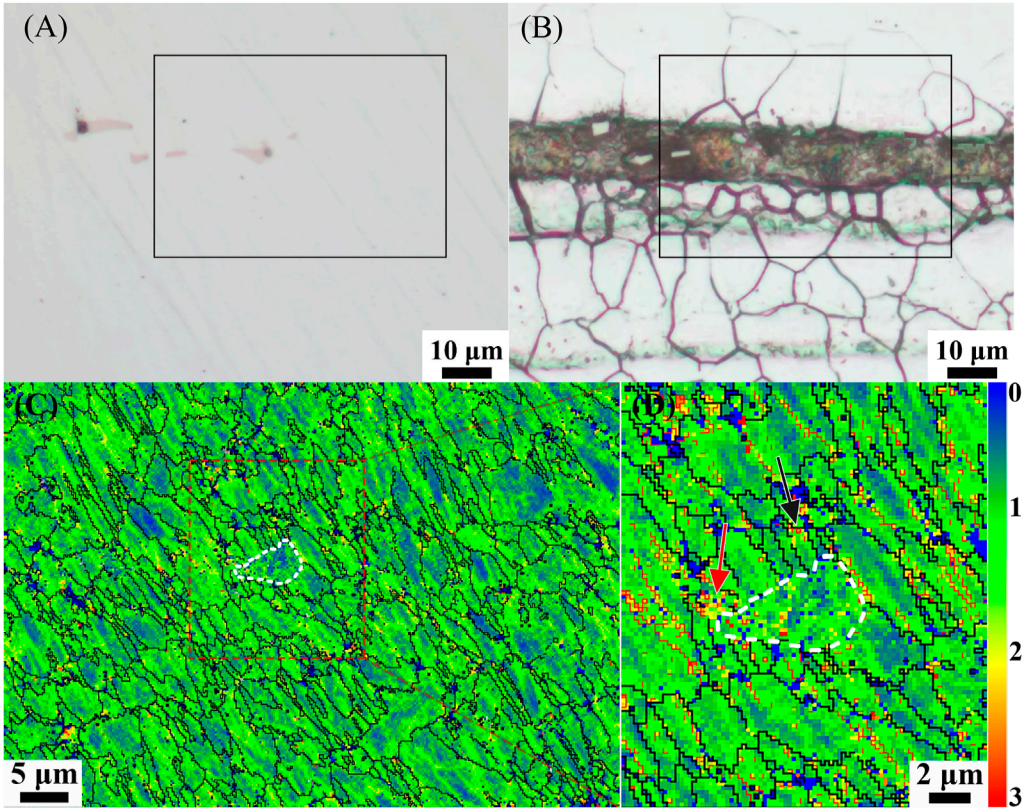

FIGURE 9
(A, B) TiN on segregation band, and **(C, D)** Kernel average misorientation map (KAM). (black line >15°, red line 2°–15°).

impact energy, abrupt temperature rise occurred and led to ASBs formation by repeated thermal softening (Baik et al., 2021). The forming of ASBs and cracks can seriously deteriorate the ballistic performance (Kim et al., 2021). It can be found from Figure 2C, D that the length of ASBs numbered from 1 to 4 around crater B was 1,633, 4,024, 4,184, 5,007 μm, respectively, while that around crater A was 1,281, 1,012, 3,946 μm, respectively. The ASB around crater B (total length, 14,848 μm) was more serious than that around crater A (total length, 6,239 μm). The different kinds of cracks were formed, following the ASBs around crater A and crater B during the ballistic impact, which were closely related to the ASBs (Chen et al., 2021; Jo et al.,

10.3389/fmats.2025.1545242

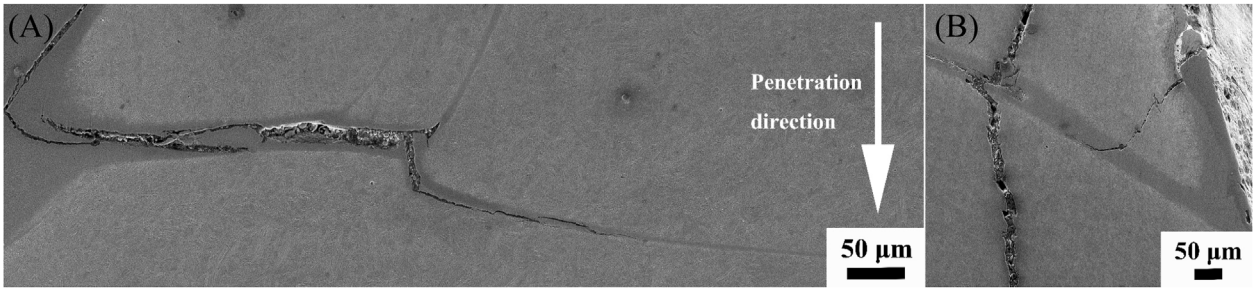

FIGURE 10
SEM images of the cracks along ASB **(A)** and intersected with ASB **(B)** in the half-sectioned area.

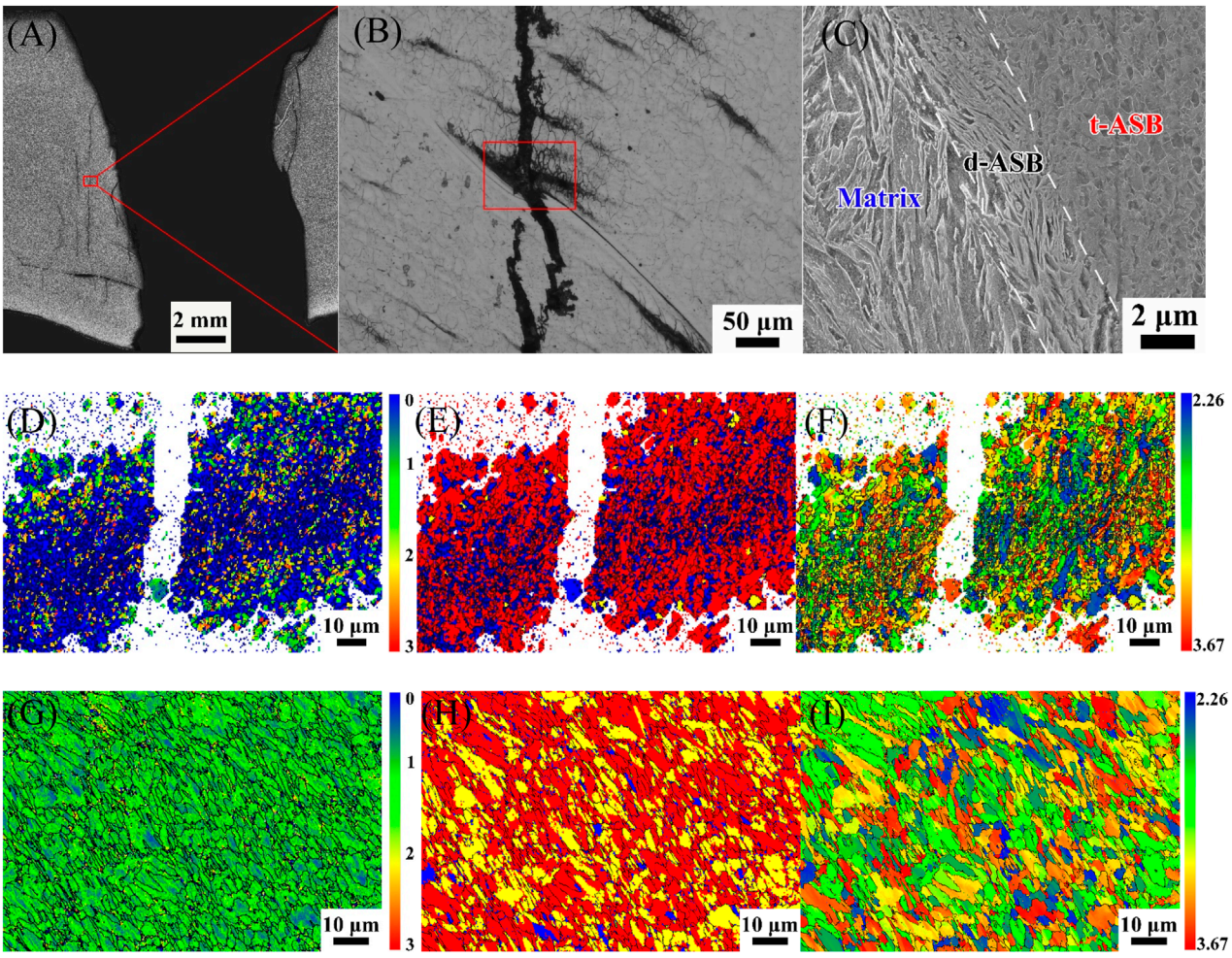

FIGURE 11
OM **(A, B)** and SEM **(C)** images in half-sectioned area in crater B **(D–F)** KAM map, distribution map of deformed grains, recrystallized grains and substructures, and TF map of ASB in red-box areas of **(B)**, and **(G–I)** KAM map, distribution map of deformed grains, recrystallized grains, and substructures, and TF map in initial steel plate. (black line >15°).

2021). A kind of crack initiated and propagated along embrittled ASBs (Figure 10A). Another kind of crack was parallel to the penetration direction, intersected with ASBs (Figure 10B). The latter only occurred around crater B with total length of 25,382 μm.

4.4 Formation mechanism of ASB and crack during ballistic impact process

In order to display the formation mechanism of ASB and crack during ballistic impact process, EBSD analysis of initial steel

plate and ASB near the crater was conducted in Figure 11. For crater B, EBSD analysis was conducted in the location of the red box in Figures 11A, B. As shown in Figure 11C, the transformed equiaxed grains in the interior of ASBs (t-ASB) and deformed grain in the exterior of ASB near matrix (d-ASB) were formed. Deformation bands was regarded as being the initial stage of localization, with further strain accumulation, t-ASB was developed from them (Yu et al., 2024).

Equiaxed grain microstructure in t-ASB was due to dynamic recrystallization resulting from the large plastic deformation (Sun et al., 2014; Li et al., 2022). From KAM map (Figure 11D), it was found that there were more bright yellow and red regions with high local strain in d-ASB, compared with that in t-ASB. At the same time, combining the distribution map of the deformed grains, recrystallized grains and substructures represented with red, blue and yellow colors, respectively (Figure 11E), it was evident that the proportion of deformed grains in d-ASB was higher than that in t-ASB, on the contrary, the proportion of recrystallized grains in t-ASB was higher than that in d-ASB. Figure 11F shows the taylor factor (TF) map, where the red color indicated high grain orientation hardness. It was evident that, compared to the t-ASB, the d-ASB displayed higher grain orientation hardness.

In a word, heavily deformed grains were observed in d-ASB near matrix, which had the typical features such as high grain orientation hardness and KAM value, as well as the high proportion of deformed grains (Figures 11D–F), tending to induce crack (Landau et al., 2016). Therefore, following cracks formed along the interfaces of d-ASB and matrix. In addition, compared with EBSD maps of initial steel plate (Figures 11G–I), it was evident that the grains of ASB was significant refined, meanwhile, along with lower KAM value and higher proportion of recrystallization grain.

It was especially obvious that much heavily deformation occurred in the matrix above ASBs with elongated grains than that below ASBs with similar equiaxed grains (Figure 11B), due to the absorption of the ballistic impact energy by the ASB formation. The inhomogeneous deformation resulted in stress concentration, especially at the interfaces of either the matrix/segregation bands or micro-sized TiN/segregation bands, making the long crack initiation and propagation under load of impact.

From Section 3.2, the specimen 1 near crater A was much less susceptible to the ASB formation than the specimen 9 near crater B, attributed to the higher *n* value and strain hardening rate (Figure 3), which can restrained the localized deformation and the final formation of ASB (Jo et al., 2020). So, the region around crater B displayed much more ASBs and cracks than that around crater A, due to the poor work hardening capability of region around crater B.

5 Conclusion

(1) The strength of the specimens near the partially penetrated crater A was slightly higher than those near the completely penetrated crater B, at the same time, the elongation, *n* value and strain hardening rate of the former was higher than that of the latter, indicating excellent strength, plasticity and deformability in the partially penetrated crater A region. The ASB with total length of 14,848 μm near completely penetrated crater B was more serious than that near partially penetrated crater A with total length of 6,239 μm, and cracks parallel to the penetration direction with total length of 25,382 μm only occurred around the completely penetrated crater B, attributed to the lower *n* value and strain hardening rate in crater B region.

(2) The segregation bands and TiN inclusions in steel plate originated from central segregation in continuous casting slabs. Almost all TiN located in segregation band in steel plate. The segregation band with fine grains and solute element enrichment in steel plate displayed high hardness, compared with the surrounding matrix. High local strain zone in the sharp corner of TiN in initial steel plate was prone to preferential initiating ASBs and cracks. At the interfaces of the matrix/segregation bands, more HAGB was found.

(3) From EBSD analysis, heavily deformed grains were observed in t-ASB near matrix, which had the typical features of high grain orientation hardness and KAM value, as well as the high proportion of deformed grains. Therefore, cracks formed along the interfaces of ASB and matrix. It was especially obvious that much heavily deformation occurred in the matrix above ASBs than that below ASBs, due to the absorption of the ballistic impact energy by the ASB formation. The inhomogeneous deformation resulted in stress concentration, especially at the interface of the matrix/segregation band and the micro-sized TiN/segregation bands, making the long crack initiation and propagation under load of impact.

Data availability statement

The original contributions presented in the study are included in the article/supplementary material, further inquiries can be directed to the corresponding author.

Author contributions

KT: Data curation, Formal Analysis, Investigation, Methodology, Validation, Writing–original draft. HS: Data curation, Methodology, Validation, Writing–review and editing. LD: Validation, Writing–review and editing. XZ: Conceptualization, Formal Analysis, Funding acquisition, Investigation, Project administration, Resources, Supervision, Writing–review and editing.

Funding

The author(s) declare that financial support was received for the research, authorship, and/or publication of this article. This research was funded by the Key R & D and Promotion Special Project of Henan Province (No. 212102210444). The funder was not involved in the study design, collection, analysis, interpretation of data, the writing of this article, or the decision to submit it for publication.

Acknowledgments

The authors gratefully acknowledge the financial support provided by the Key R & D and Promotion Special Project of Henan Province (No. 212102210444).

Conflict of interest

The authors declare that the research was conducted in the absence of any commercial or financial relationships that could be construed as a potential conflict of interest.

Generative AI statement

The author(s) declare that no Generative AI was used in the creation of this manuscript.

Publisher's note

All claims expressed in this article are solely those of the authors and do not necessarily represent those of their affiliated organizations, or those of the publisher, the editors and the reviewers. Any product that may be evaluated in this article, or claim that may be made by its manufacturer, is not guaranteed or endorsed by the publisher.

References

Baik, S.-I., Gupta, R. K., Kumar, K. S., and Seidman, D. N. (2021). Temperature increases and thermoplastic microstructural evolution in adiabatic shear bands in a high-strength and high-toughness 10 wt.% Ni steel. *Acta Mater* 205, 116568. doi:10.1016/j.actamat.2020.116568

Bee, C., Slater, C., Davis, C., and Farrugia, D. (2023). Micro-Segregation induced strain inhomogeneity in >900 MPa UTS martensitic hot rolled advanced high strength steel. *Mater. Sci. Eng. A* 888, 145335. doi:10.1016/j.msea.2023.145335

Bertolo, V., Vilasi, L., Jiang, Q., Riemslag, T., Scott, S., Walters, C. L., et al. (2023). Grain refinement by rapid cyclic heating and its effect on cleavage fracture behaviour of an S690 high strength steel. *J. Mater. Res. Technol.* 23, 1919–1933. doi:10.1016/j.jmrt.2023.01.164

Borvik, T., Dey, S., and Clausen, A. H. (2009). Perforation resistance of five different high-strength steel plates subjected to small-arms projectiles. *Int. J. Impact Eng.* 36 (7), 948–964. doi:10.1016/j.ijimpeng.2008.12.003

Borvik, T., Langseth, M., Hopperstad, O. S., and Malo, K. A. (2002). Perforation of 12 mm thick steel plates by 20 mm diameter projectiles with flat, hemispherical and conical noses Part I: experimental study. *Int. J. Impact Eng.* 27 (1), 19–35. doi:10.1016/s0734-743x(01)00034-3

Chausov, M., Maruschak, P., Pylypenko, A., Shmanenko, V., Brezinová, J., and Lisnichuk, M. (2024). The effects of cryogenic treatment and impact-oscillatory loading on changes in the mechanical properties and structural condition of stainless steel 12Kh18N10T. *Mater. Sci. Eng. A* 913, 147007. doi:10.1016/j.msea.2024.147007

China National Standard (2021). *Mechanical properties of metals-tensile testing-part 1: method of test at room temperature (GB/T 228.1-2021)*. Beijing: China National Standard.

Chen, J., Bao, K., Zhang, X., Cao, Y., Peng, Y., Kong, J., et al. (2021). Adiabatic shear band development and following failure in 316L fabricated by an additive manufacturing process. *Mater. Sci. Eng. A* 811, 141003. doi:10.1016/j.msea.2021.141003

Guo, F., Wang, X., Wang, J., Misra, R. D. K., and Shang, C. (2020). The significance of central segregation of continuously cast billet on banded microstructure and mechanical properties of section steel. *Metals* 10 (1), 76. doi:10.3390/met10010076

He, J., Niu, F., Zuo, X., Liu, D., and Cai, M. (2022). Changes in microstructure and mechanical properties during the bending process of NM450 wear-resistant steel. *Mater. Res. Express* 9 (4), 046524. doi:10.1088/2053-1591/ac68d6

Jo, M. C., Kim, S., Suh, D. W., Hong, S. S., Kim, H. K., Sohn, S. S., et al. (2020). Effect of tempering conditions on adiabatic shear banding during dynamic compression and ballistic impact tests of ultra-high-strength armor steel. *Mater. Sci. Eng. A* 792, 139818. doi:10.1016/j.msea.2020.139818

Jo, M. C., Kim, S., Suh, D. W., Kim, H. K., Kim, Y. J., Sohn, S. S., et al. (2021). Enhancement of ballistic performance enabled by transformation-induced plasticity in high-strength bainitic steel. *J. Mater. Sci. Technol.* 84, 219–229. doi:10.1016/j.jmst.2020.12.059

Kim, S., Jo, M. C., Suh, D. W., Kim, H. K., Sohn, S. S., and Lee, S. (2021). Suppression of adiabatic shear band formation by martensitic transformation of retained austenite during split Hopkinson pressure bar test for a high-strength bainitic steel. *Mater. Sci. Eng. A* 814, 141127. doi:10.1016/j.msea.2021.141127

Landau, P., Osovski, S., Venkert, A., Gartnerova, V., and Rittel, D. (2016). The genesis of adiabatic shear bands. *Sci. Rep.* 6, 37226. doi:10.1038/srep37226

Li, X.-Y., Zhang, Z.-H., Cheng, X.-W., Wang, Q., Jia, X.-T., Wang, D., et al. (2022). The evolution of adiabatic shear band in high Co-Ni steel during high strain-rate compression. *Mater. Sci. Eng. A* 858, 144173. doi:10.1016/j.msea.2022.144173

Liang, G., Liu, Y., Yang, X., Atrens, A., Wu, T., Tian, Z., et al. (2023). Grain refinement of A517 steel by inoculation with Al-5Ti-B master alloy. *Mater. Chem. Phys.* 296, 127320. doi:10.1016/j.matchemphys.2023.127320

Liu, D., Wang, Z., Liu, J., Wang, Z., and Zuo, X. (2022). Study of the fracture behavior of TiN and TiC inclusions in NM550 Wear-Resistant steel during the tensile process. *Metals* 12 (2), 363. doi:10.3390/met12020363

Liu, T., Long, M.-j., Chen, D.-f., Duan, H.-m., Gui, L.-t., Yu, S., et al. (2018). Effect of coarse TiN inclusions and microstructure on impact toughness fluctuation in Ti microalloyed steel. *J. Iron Steel Res. Int.* 25 (10), 1043–1053. doi:10.1007/s42243-018-0149-5

Ma, X., Miao, C., Langelier, B., and Subramanian, S. (2017). Suppression of strain-induced precipitation of NbC by epitaxial growth of NbC on pre-existing TiN in Nb-Ti microalloyed steel. *Mater. Des.* 132, 244–249. doi:10.1016/j.matdes.2017.07.006

Maruschak, P., and Maruschak, O. (2024). Methods for evaluating fracture patterns of polycrystalline materials based on the parameter analysis of fatigue striations: a review. *Methodsx* 13, 102989. doi:10.1016/j.mex.2024.102989

McDonald, B., Bornstein, H., Ameri, A., Daliri, A., and Orifici, A. C. (2019). Plasticity and ductile fracture behaviour of four armour steels. *Int. J. Solids Struct.* 176-177, 135–149. doi:10.1016/j.ijsolstr.2019.05.013

Narasaiah, N., and Ray, K. K. (2005). Small crack formation in a low carbon steel with banded ferrite-pearlite structure. *Mater. Sci. Eng. A* 392 (1-2), 269–277. doi:10.1016/j.msea.2004.09.058

Pan, T., Yang, Z. G., Bai, B. Z., and Fang, H. S. (2003). Study of thermal stress and strain energy in γ-Fe matrix around inclusion caused by thermal coefficient difference. *Acta Metall. Sin.* 39 (10), 1037–1042. doi:10.3321/j.issn:0412-1961.2003.10.005

Shi, Z., Li, J., Zhang, X., Shang, C., and Cao, W. (2022). Influence mechanisms of inclusion types on rotating bending fatigue properties of SAE52100 bearing steel. *Materials* 15 (14), 5037. doi:10.3390/ma15145037

Singh, B. B., Sukumar, G., Paman, A., Balaji, G., Siva Kumar, K., Madhu, V., et al. (2021). A comparative study on the ballistic performance and failure mechanisms of high-nitrogen steel and RHA steel against tungsten heavy alloy penetrators. *J. Dyn. Behav. Mater.* 7 (1), 60–80. doi:10.1007/s40870-020-00270-8

Singh, B. B., Sukumar, G., Rao, P. P., Kumar, K. S., Madhu, V., and Kumar, R. A. (2019). Superior ballistic performance of high-nitrogen steels against deformable and non-deformable projectiles. *Mater. Sci. Eng. A* 751, 115–127. doi:10.1016/j.msea.2019.02.044

Sun, H., Du, H., Tong, K., Liu, L., Yan, Q., and Zuo, X. (2023). Influence of TiN inclusions and segregation bands on the mechanical properties and delayed crack in thick NM550 wear-resistant steel. *Materials* 16 (17), 5856. doi:10.3390/ma16175856

Sun, X., Wang, H., Yang, P., and Mao, W. (2014). Mechanical behaviors and micro-shear structures of metals with different structures by high-speed compression. *Acta Metall. Sin.* 50 (4), 387–394. doi:10.3724/sp.J.1037.2013.00634

Teixeira, J., Moreno, M., Allain, S. Y. P., Oberbillig, C., Geandier, G., and Bonnet, F. (2021). Intercritical annealing of cold-rolled ferrite-pearlite steel: microstructure evolutions and phase transformation kinetics. *Acta Mater* 212, 116920. doi:10.1016/j.actamat.2021.116920

Wang, J. L., Qian, R. T., Yang, X., Zhong, Y., and Shang, C. J. (2022). Effect of segregation on the microstructure and properties of a quenching and partitioning steel. *Mater. Lett.* 325, 132815. doi:10.1016/j.matlet.2022.132815

Wang, S., Li, C., Zheng, M., Ye, Z., Zhong, H., Tong, D., et al. (2020). *In-situ* deformation characterization of mesosegregated high-strength low-alloy steel. *Mater. Charact.* 169, 110627. doi:10.1016/j.matchar.2020.110627

Wang, Z., Wu, X., Liu, D., and Zuo, X. (2021). Correlation between microstructure and fracture behavior in thick HARDOX 450 wear-resistant steel with TiN inclusions. *Front. Mater.* 8, 691551. doi:10.3389/fmats.2021.691551

Wu, X., Zuo, X., Zhao, W., and Wang, Z. (2020). Mechanism of TiN fracture during the tensile process of NM500 wear-resistant Steel. *Acta Metall. Sin.* 56 (2), 129–136. doi:10.11900/0412.1961.2019.00209

Yilmaz, A. (2010). Development of an armor steel for ballistic protection. *Mater. Test.* 52 (11-12), 811–818. doi:10.3139/120.110190

Yu, Y., Zhang, Y., Xu, S., Han, J., Li, J., Guo, C., et al. (2024). High-strain-rate deformation of a nanoprecipitate-strengthened dual-phase steel. *Int. J. Plast.* 173, 103887. doi:10.1016/j.ijplas.2024.103887

Zhang, R., Zheng, C., Bo, L., Chen, C., Zhang, P., and Zhang, F. (2022). *In-situ* investigation of composition segregation and deformation streamline in bainitic steel on mechanical properties. *Mater. Sci. Eng. A* 855, 143949. doi:10.1016/j.msea.2022.143949

Zhang, W., Wu, J., Wen, Y., Ye, J., and Li, N. (2010). Characterization of different work hardening behavior in AISI 321 stainless steel and Hadfield steel. *J. Mater. Sci.* 45 (13), 3433–3437. doi:10.1007/s10853-010-4369-8